Check for updates

Synthesis and optical spectroscopy of Na₃Y(VO₄)₂:Eu³⁺ phosphors for thermometry and display applications†

Ikhlas Kachou,[a] Kamel Saidi, [ID] [a] Rached Salhi[bc] and Mohamed Dammak [ID] *[a]

A new $Na_3Y(VO_4)_2$:Eu^{3+} (NYVO:Eu^{3+}) phosphor was prepared using the sol–gel method. X-ray diffraction (XRD) and scanning electron microscopy (SEM) were used to evaluate phase purity and particle size, respectively. The optical properties were investigated by UV-visible absorption, PL, and PLE spectroscopies. The absorption measurements show the formation of the vanadate host by the presence of its characteristic band in the visible region related to VO_4^{3-} groups. The experimental results show that the NYVO:Eu^{3+} phosphors exhibit high-brightness and thermally stable emission. Under near-ultraviolet (UV) excitation, both the broadband emission from VO_4^{3-} groups and the sharp peak emissions from Eu^{3+} ions are observed. The highest luminescence intensity was achieved for an optimal europium concentration of 15 mol%. The study of the chromaticity parameters of these compounds gives a thermally stable hot emission in the red domain, with a color purity of about 85%, which qualifies the NYVO:Eu^{3+} compound as a potential phosphor for light-emitting diode (LED) applications. Thermal sensing using NYVO:Eu^{3+} phosphors are based on monitoring the luminescence intensity ratio between the NYVO host emission and Eu^{3+} luminescence lines. Notably, the optical thermometry of NYVO:Eu^{3+} was characterized based on the fluorescence intensity ratio of VO_4^{3-} and Eu^{3+} emissions in the 298–440 K range, with maximum absolute and relative sensitivities of 3.4% K^{-1} and 0.0032 K^{-1} respectively and a temperature uncertainty of 0.01. NYVO:Eu^{3+} can then be considered as a potential red phosphor for application in ultraviolet-pumped white light-emitting diodes and as a potential optical thermometer. It provides new possibilities for the design of multifunctional materials for red light-emitting diodes and for non-contact thermometry.

1. Introduction

Rare earth doped phosphors have been widely used in recent years in a variety of applications, ranging from light sources and displays to catalysts and biomarkers.[1–5] Contactless optical thermometry has recently received a lot of interest as a novel approach with great detection sensitivity, spatial resolution, and a short acquisition time.[6–10] Contactless optical thermometry has recently received a lot of interest as a novel approach with great detection sensitivity, spatial resolution, and a short acquisition time. Hence, diverse optical materials have been used in contactless optical thermometry ranging from MOFs, glass, polycrystals, and their composites. Among them,

phosphors are of great interest for this purpose, especially considering their low cost, easy preparation and morphology ranging from nano-to micro range.[11,12] Highly sensitive thermometers are in great demand in a range of sectors such as nanomedicine, integrated photonic devices, microfluidics, and nanoelectronics.[7,13–15] The luminescence intensity ratio (LIR) temperature measuring strategy is to calibrate the temperature using the relative emission peaks ratio.[16] The fluorescence intensities ratio of multiple thermal coupling energy levels in a single light-emitting center is the standard LIR temperature measuring method. This temperature monitoring technique is harmful to getting increased relative and absolute sensitivity at the same time, and it has an impact on signal resolution. This restriction can be surmounted using the LIR between emissions bands associated with distinct active centers. Currently, phosphors doped with lanthanides are widely used in LIR temperature measurement systems. Optical thermometric characterization using the LIR technique with codoped or doped with rare earth and transition metal ions has been reported in several reports: $K_3Gd(VO_4)_2$:Tb^{3+}/Sm^{3+}[17] $NaGd(MoO_4)_2$:Tb^{3+}/Pr^{3+},[18] $Y_3Al_5O_{12}$:RE/TM (TM = Mn^{4+}, Cr^{3+}, RE = Eu^{3+}, Tb^{3+}, Dy^{3+}),[19] $Na_4Mg(WO_4)_3$:Tb^{3+}/Mn^{4+},[20] and

aLaboratoire de Physique Appliquée, Groupe de Physique des Matériaux Luminescents, Faculté des Sciences de Sfax, Département de Physique, Université de Sfax, BP 1171, 3018, Sfax, Tunisia. E-mail: madidammak@yahoo.fr; mohamed.dammak@fss.usf.tn

bLaboratory of Advanced Materials, National School of Engineers of Sfax, Sfax University, 3018 Sfax, Tunisia

cUniv Grenoble Alpes, CNRS, Grenoble INP, LMGP, Grenoble France Institute of Engineering Univ, Grenoble, 38000, France

$Na_3Y(PO_4)_3$:Dy.[21] In the LIR technique, the matrix material is usually crucial in determining the temperature-sensing performance. Based on the above assumption, selecting the right luminous host material, especially one with low phonon energies, is essential for ensuring that RE ions have good luminescent characteristics and may be used in a variety of applications.

Vanadates are regarded as an excellent luminescent host materials for RE ions that have been widely investigated for solid-state lighting, solar cells, and optical displays, because of their strong absorption in the near-ultraviolet (NUV) region and good intrinsic emissions originating from the electronic transitions of $^3T_J - {}^1A_1$ ($J = 1, 2$) in the VO_4^{3-} group.[22] Recently, several researches focused on the double vanadate doped with various lanthanides ions, such as Er^{3+}, $Na_3Gd(VO_4)_2$:Ho^{3+}/Yb^{3+},[23] $Na_3Y(VO_4)_2$:Sm^{3+},[24] $Na_3Y(VO_4)_2$:Tm^{3+},[25] $K_3Y(VO_4)_2$:Ln (Ln = Eu, Er, Sm, Ho, Tm).[26]

In this work, Eu^{3+}-doped $Na_3Y(VO_4)_2$ phosphors are synthesized *via* a sol gel method. The crystal structure is examined by X-ray diffraction (XRD). The room temperature photoluminescence properties for varied concentrations, the luminescence properties and the chromaticity parameters are investigated. Ultimately, by evaluating the varied temperature responses of the VO_4^{3-} group and Eu^{3+} ions, the temperature sensing behaviors of the NYVO phosphors were investigated and their performances are evaluated *via* the S_a and S_r parameters.

2. Experimental methods

2.1 Synthesis of the phosphor

A series of europium doped NYVO nanocrystals ($Na_3Y_{1-x}Eu_x(VO_4)_2$) ($x = 0, 0.05, 0.1, 0.15$ and 0.20) were synthesized by combustion route method-based citrate *via* low temperature. Analytical grade ammonium vanadate (NH_4VO_3), sodium hydroxide (NaOH), citric acid monohydrate ($C_6H_8O_7$) and high purity yttrium nitrate hexahydrate ($Y(NO_3)_3 \cdot 6H_2O$ (99.9%)) and europium trinitrate pentahydrate ($Eu(NO_3)_3 \cdot 5H_2O$ (99.9%)) were used as the starting materials. Firstly, all the precursors are placed in an Erlenmeyer and dissolved in ionized water under magnetic stirring at 70 °C. Next, citric acid is added and the color of the solution turns from green to blue. The solution was continued swirling and heated at 80 °C until it hydrolyzed into a sol and then a gel. Finally, the gel will be heated for calcination by annealing at 500 °C. The final products were reground for further characterization.

2.2 Characterization

The powder X-ray diffraction (PXRD) patterns of the sample were performed at room temperature using a powder X-ray D8-Advance Bruker diffractometer, with monochromatic copper radiation CuKα1 ($\lambda = 1.5406$ Å) a step size of 0.015° from 10° to 75°, running at 45 kV and 40 mA. The phase purity is cheeked using the Fullprof program. The morphologies of the samples were investigated using a Zeiss Supra55VP FEG-SEM scanning electron microscopy (SEM) with an accelerating voltage of 2–8 kV and a Bruker XFlash 5030. UV-vis-NIR absorption was determined using a UV-vis-NIR spectrometer (PerkinElmer Lambda 950). The photoluminescence excitation (PLE) and photoluminescence (PL) spectrum was measured using a Jobin Yvon Fluoromax-4 Spectrofluorometer (Horiba, USA) with a 150 W Xe lamp as a source of excitation. An Easy Life-Horiba instrument was employed to measure the emission lifetime. The light source was a 375 nm diode laser.

3. Results and discussion

3.1 XRD analysis

The crystal structure and phase purity of the samples were analyzed using XRD patterns. Fig. 1 shows the X-ray diffraction (XRD) patterns recorded in 10°–75° 2θ range of the nanocrystals NYVO:xEu^{3+} with $x = 0., 0.05, 0.10, 0.15$, and 0.20. The samples are shown to have a monoclinic structure based on the NYVO XRD patterns (JCPDS no. 70-0257), with $P2_1/n$ space group no 14 ($Z = 2$) and which is isomorphous with $Na_3Er(VO_4)_2$.[27] The X-ray diffraction peaks were quite similar for the undoped and doped NYVO, showing that the phase of the sample remained unchanged after Eu^{3+} doping. In the NYVO crystal, the Eu^{3+} ions ($r = 0.947$ nm) replace the crystallographic position of the Y^{3+} ions ($r = 0.9$ nm). The sites of the Y^{3+} and Eu^{3+} ions are of C_{2v} symmetry. The point symmetry of the $(VO)_4^{3-}$ anions is C_1. The X-ray diffraction patterns were extremely similar, confirming that the phase prototype remained relatively stable after doping. The comparison with the experimental pattern and the simulated one from the X-ray data confirmed the purity of the synthesized powder. Moreover, the powder X-ray pattern was fitted by Le Bail refinement method. The refinement resulted in an excellent match between the experimental and estimated patterns (Fig. S1(a–e)†), indicating that the produced powder was pure. The obtained unit cell parameters are closer to those obtained from single crystal data. Le Bail refinement parameters of all phosphors are given in Table S1.†

3.2 Morphology characterization

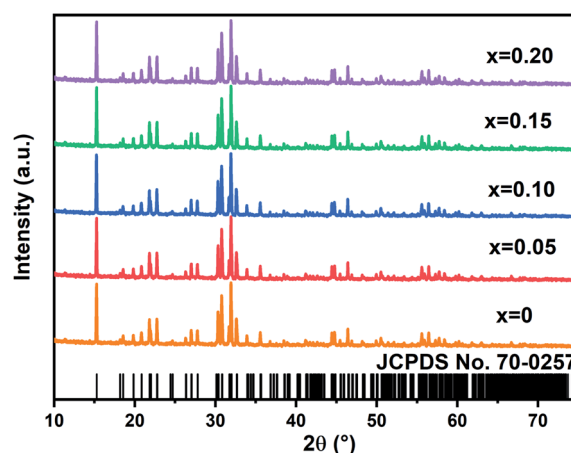Fig. 2 shows a SEM image of NYVO:xEu^{3+} with $x = 0$ and 0.15 phosphor produced at 500 °C. The agglomerated and irregularly

Fig. 1 XRD of the NYVO:xEu^{3+}($x = 0, 0.05, 0.1, 0.15$ and 0.20).
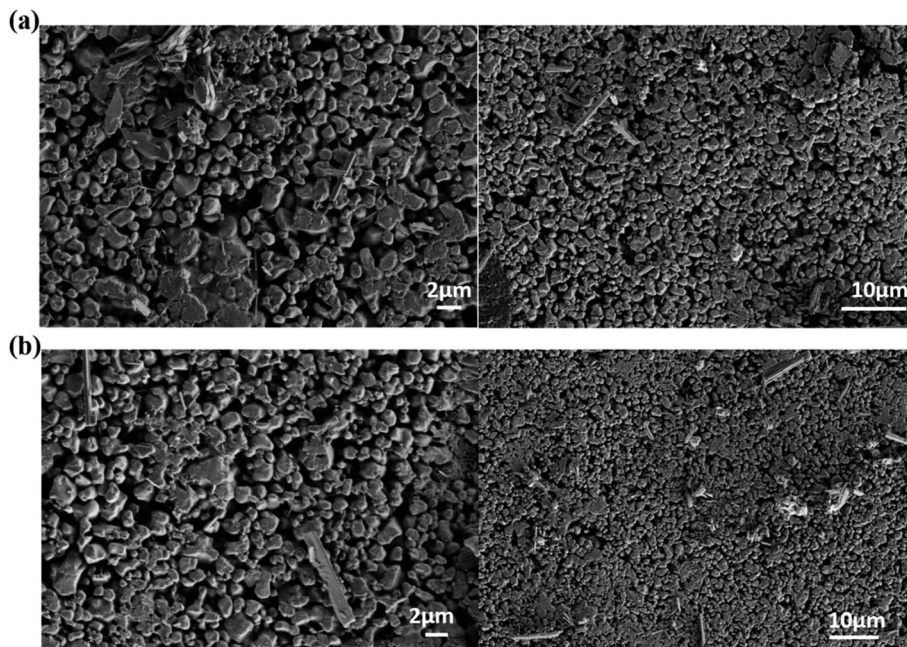
Fig. 2 (a) SEM image of NYVO, (b) SEM image of NYVO:0.15Eu^{3+}.

shaped particles are seen in the micrographs. The average diameter of the grain size is in the region of 500–800 nm. According to published research, phosphor powder with agglomeration and morphology can reduce the effective light-emitting area and packing density.[28]

4.   Optical characterizations

4.1   UV-vis absorption

The diffuse reflectance spectrum (Fig. 3a) of NYVO:xEu^{3+} (x = 0.05, 0.1, 0.15 and 0.2) phosphors in the 200–800 nm range. The large band in 240–370 nm range is attributed to the charge transfer from the 2p oxygen orbital to 3d vanadium orbital of the (VO$_4$)$^{3-}$ group.

The Kubelka–Munk (KM) theory was used to calculate the band gap of NYVO phosphor using diffuse reflectance spectra. The relation between the diffuse reflectance of the sample (R_∞),

absorption coefficient (K) and scattering coefficient (S) are related by the KM remission function $F(R_\infty)$:[6,29]

$$F(R) = \frac{K}{S} = \frac{(1-R)^2}{2R} \tag{1}$$

In the parabolic band structure, the band gap E_g and absorption coefficient α of a direct band gap semiconductor are related through the well-known Tauc equation:[6]

$$((F(R)h\nu)^n) = B\,(h\nu - E_g) \tag{2}$$

The plot of $[F(R_\infty)h\nu]^2$ versus $h\nu$ (Fig. 3b) exhibits nonlinear and linear portions, which is the characteristic of direct allowed transition. The nonlinear portion corresponds to a residual absorption involving impurity states and the linear portion characterizes the fundamental absorption. The value of E_g of
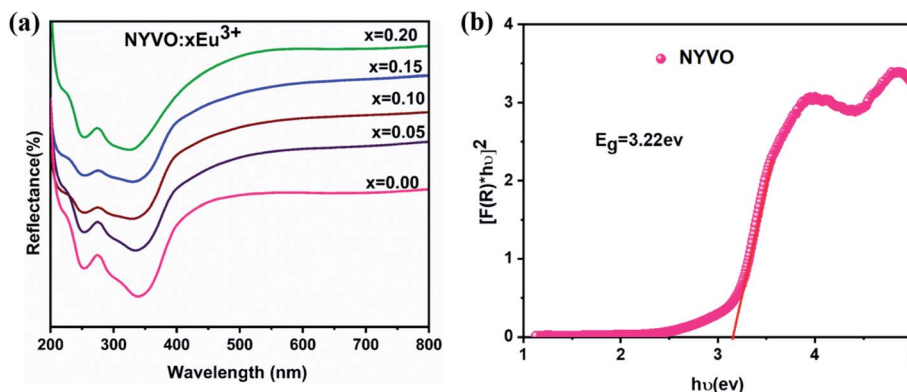

Fig. 3 (a) Diffuse reflectance spectra of NYVO:xEu^{3+}(x = 0.00, 0.0 5, 0.10, 0.15 and 0.20) (b) the plot of $[F(R_\infty)h\nu]^2$ versus $h\nu$ of NYVO.
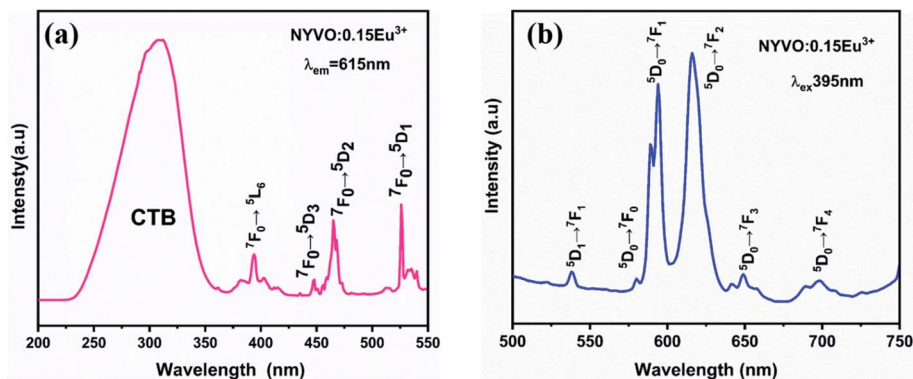
Fig. 4 (a) Excitation spectra monitored at λ_{em} = 615 nm (b) emission spectra measured at λ_{ex} = 395 nm excitation of NYVO:0.15Eu^{3+}.

NYVO was obtained (3.22 eV) by extrapolating the straight line to $[F(R_{\infty})h\nu]^2 = 0$. The energy gap values $h\nu$ of the NYVO:xEu^{3+} (Fig. S2†) were calculated to be: 3.19, 3.18, 3.17 and 3.15 eV for x = 0.5, 0.10, 0.15, and 0.2, respectively. The energy of the gap decreases from 3.22 to 3.15 eV as the doping rates increase. These results also indicate that there is no significant change in the energy of the band gap when the europium ions are incorporated into the NYVO host matrix.

4.2 Photoluminescence properties

To gain a better understanding of the potential of the produced powder as a novel phosphor, a complete and systematic research of the photoluminescence excitation and emission of Eu^{3+} doped NYVO was carried out.

Fig. 4a shows the excitation spectrum of the luminescence (PLE) of NYVO:0.15Eu^{3+} monitored at λ_{em} = 615 nm. The PLE spectrum displays a wide band, in the 250–380 nm range, which can be attributed to the $V^{5+} \rightarrow O^{2-}$ charge transfer (CT) transitions of the $(VO_4)^{3-}$ group. Other excitation peaks between 350 nm and 550 nm correspond to the intra-configuration 4f–4f electronic transition of Eu^{3+} ions. These peaks are attributed to the transitions from the $^7F_0$ fundamental level to the $^5L_7$ (382 nm), $^5L_6$ (395 nm), $^5D_3$ (417 nm), $^5D_2$ (465 nm) and $^5D_1$ (525 nm) excited levels.[30] The emission spectra of NYVO:0.15Eu^{3+} (Fig. 4b) upon 395 nm excitation exhibit the typical emission peaks of the Eu^{3+} ion corresponding to the $^5D_0 \rightarrow {}^7F_0$, $^5D_0 \rightarrow {}^7F_1$, $^5D_0 \rightarrow {}^7F_2$, $^5D_0 \rightarrow {}^7F_3$, and $^5D_0 \rightarrow {}^7F_4$ transitions situated at about 579, 593, 615, 648, and 697 nm, respectively.[31] The $^5D_0$–^7F_J emission lines of Eu^{3+} ions have the advantage of being able to investigate the local site symmetry of optically active centers.[32] The $^5D_0 \rightarrow {}^7F_0$ transition is an electric-dipole transition, which strictly prohibited by the selection rules. It can only be observed in a C_n, C_{nv} or C_s type distorted environment. Thus, the presence of this transition on the emission spectrum provides information on the number of non-centrosymmetric sites in which the Eu^{3+} ion is found.[33] The $^5D_0 \rightarrow {}^7F_1$ transition is a magnetic-dipole transition with an intensity that is generally independent of the Eu^{3+} ion's surrounding chemical environment. It is dominant if the Eu^{3+} ions are localized in a centrosymmetric site. While the electric dipole transition $^5D_0 \rightarrow {}^7F_2$ is hypersensitive to the environment. It will become the dominant transition if

the Eu^{3+} ions maintain a site without a center of inversion. From the emission spectrum (Fig. 4b), it is clear that the $^5D_0 \rightarrow {}^7F_2$ transition is the strongest emission, indicating that the Eu^{3+} ions occupy an asymmetric environment in NYVO host.

Fig. 5 depicts the emission spectra of NYVO:0.15Eu^{3+} at various excitation wavelengths (320 nm, 395 nm, and 465 nm). For various excitations, the emission peak positions stay unchanged. From the PL spectra, we observe that the highest intensity of transition $^5D_0 \rightarrow {}^7F_2$ is obtained upon 395 nm excitation. But when excited at 320 nm, we observe that the $^5D_0 \rightarrow {}^7F_1$ emission intensity dominates the $^5D_0 \rightarrow {}^7F_2$ emission which could be explained by the energy transfer between the $(VO_4)^{3-}$ vanadate entities and the Eu^{3+} ions.

Fig. 6 shows the photoluminescence spectra of the NYVO:xEu^3 phosphors with varying Eu^{3+} doping concentrations. For 0.15 mol Eu^{3+} dopage concentration, the PL intensity increased to its maximum value and then decreased for higher Eu^{3+} concentrations, indicating that x = 0.15 is the optimum concentration quenching in the NYVO phosphor.

For 5% and 10% Eu^{3+} concentrations the $^5D_0 \rightarrow {}^7F_1$ magnetic-dipole transition dominates the emission spectra of
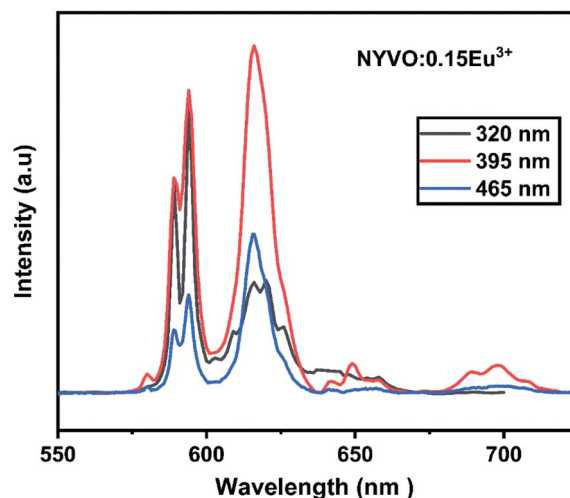

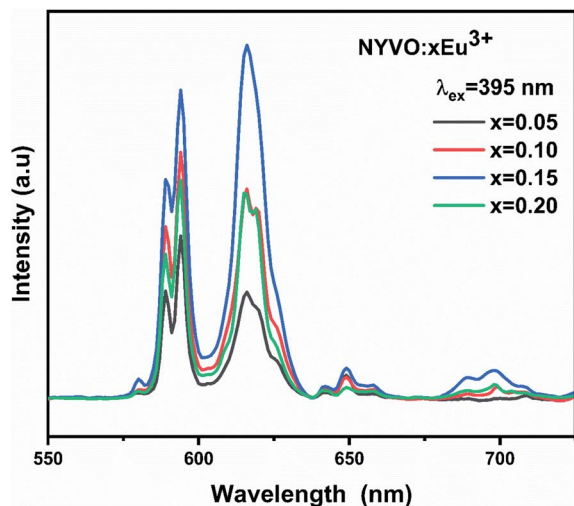**Fig. 5** Emission spectra of NYVO:0.15Eu^{3+} upon different excitation wavelengths.

Fig. 6 Emission spectrum of NYVO:xEu^{3+} (x = 0.05, 0.10, 0.15 and 0.20) excited at 395 nm.

Fig. 7 Relations between the log(I/x) and log(x) in NYVO:xEu^{3+}.

the phosphor under 395 nm excitation which indicates that in this case the Eu^{3+} are located at non inversion symmetry site. However, for 15% Eu^{3+} concentration the $^5D_0 \rightarrow {}^7F_2$ electric-dipole transition dominates the emission spectrum. For higher (20%) Eu^{3+} concentrations, the two emission intensity peaks decrease due to quenching phenomena obtained by Eu^{3+}–Eu^{3+} energy transfer.

To explore the reason for concentration quenching, the critical distance (R_c) among doped Eu^{3+} ions are calculated using the equation presented by Blass.[34,35]

$$R_c = 2\left[\frac{3V}{4\pi x_c N}\right]^{1/3} \tag{3}$$

where the volume (V) = 387.81 Å^3, the critical concentration x_c = 0.15, and N = 2 is the number of Eu^{3+} ions per unit cell. As a result, the critical distance (R_c) was calculated to be around 13.51 Å which is higher than 5 Å. This R_c value corresponds to a multipolar interaction, which is the only mechanism responsible for non-radiative energy transfer. The following equation explains the relationship between luminescent intensity and doping concentration.[5,36]

$$\frac{I}{X} = k\left(1 + \beta(x)^{\theta/3}\right)^{-1} \tag{4}$$

where I represent the emission intensity, k and β are related to the coefficients, and Q represents the interaction type constant. In addition, equivalence to eqn (3) could also be expressed as:

$$(I/X) = -(\theta/3)L(X) + A \tag{5}$$

Fig. 7 exhibits the concentration relationship curve (log(I/x) − log x), with Eu^{3+} concentrations. We thus obtain an affine line with a slope equal to 0.77 and the value of θ equal to 2.4, which corresponds approximately to the value 3. This indicates that the energy transfer is caused by the dipole–dipole interaction type (D–D).
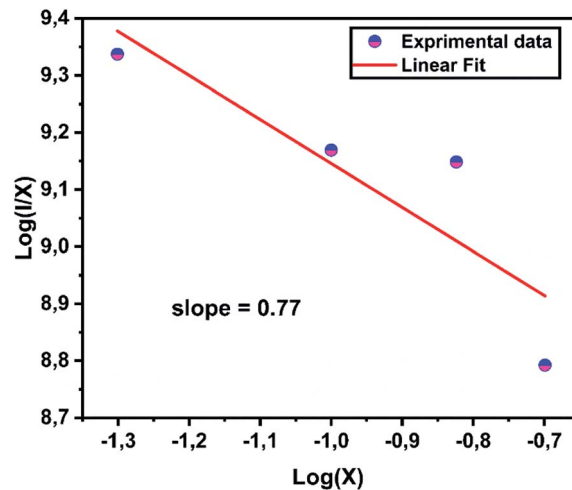
The lanthanides-activated phosphors' emission decay curves were also studied, and the correlation of activator concentration on luminescence characteristics and decay duration might strongly support concentration quenching in the energy migration process. Fig. 8 shows the logarithmic intensity emission decay curves of red emissions at 612 nm in NYVO:xEu^{3+} (x = 0.5, 0.10, 0.15, and 0.2) phosphors under 375 nm excitation. The monitored curves for NYVO:xEu^{3+} can be well fitted by a single exponential expression, as described below:

$$I(t) = A + I_0 e^{(-t/\tau)} \tag{6}$$

where I is the emission intensity at time t; I_0 refers to the initial emission intensity; A is a constant; and τ represents the decay lifetime. Then, the luminescence decay of the NYVO:xEu^{3+} samples (Fig. S4†) were calculated to be: 0.356, 0.358, 0.368 and 0.351 ms for x = 0.5, 0.10, 0.15, and 0.2, respectively. Clearly, the
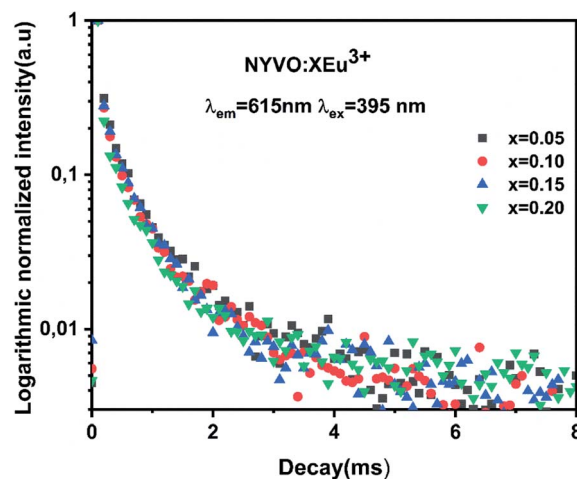

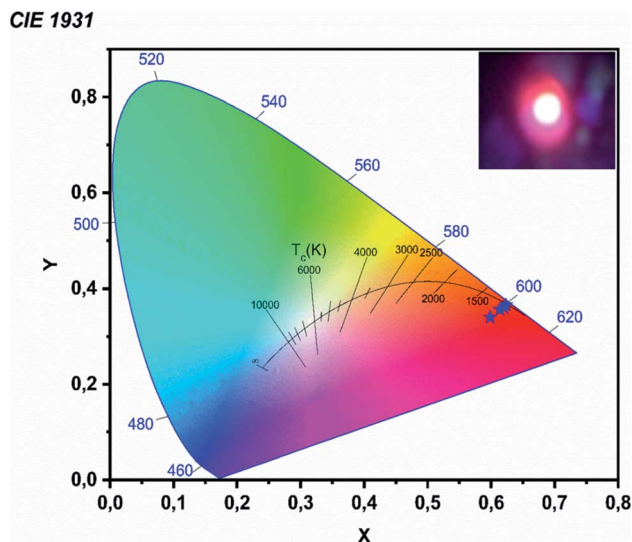Fig. 8 Room temperature fluorescence decay curves of NYVO doped with 0.05, 0.1, 0.15 and 0.2 of Eu^{3+}.

Fig. 9 CIE chromaticity diagram of NYVO:xEu^{3+} λ_{exc} = 395 nm.

Table 1 Chromaticity coordinates and CCT color temperature for the NYVO:xEu^{3+} obtained for different Eu^{3+} concentrations

Doping concentration (x)	x	y	CCT	Color purity (%)
0.05	0.5985	0.3402	2156	79
0.10	0.6137	0.3563	2040	84
0.15	0.6201	0.3607	2033	86
0.20	0.6237	0.3656	1998	85

decay lifetimes exhibited a reduced trend with the increase of Eu^{3+} doping concentration, which can be attributed to the enhanced probability of non-radiative energy transfer among Eu^{3+} activators in NYVO:xEu^{3+} phosphors.

The single decay time suggested the uniform chemical environment of Eu^{3+} ions in the NYVO host, which was also consistent with the structure analysis that there is one sort of Eu^{3+} emission center in the phosphor. It was confirmed that the lifetime values increased monotonically and reached a maximum at x = 0.15. The concentration quenching effect is demonstrated in this study with Eu^{3+}-dopant concentrations surpassing 15 mol%. As a result, the decay times of as-synthesized phosphors remain practically unaltered, owing to the minimal energy immigration between Eu^{3+} ions.

Color coordinates are used to compare phosphors. The chromaticity coordinates of NYVO:xEu^{3+} phosphors are estimated from the emission spectra and are displayed in Fig. 9. The color purity is an important parameter, which could be calculated by using the following equation, according to the literature.[37,38]

$$\text{Cpp} = \frac{\left(\sqrt{(x - x_i)^2 + (y - y_i)^2} \right)}{\sqrt{(x_d - x_i)^2 - (y_d - y_i)^2}} 100\% \tag{7}$$

Here, (x, y) is the CIE coordinate of the samples, (x_i, y_i): the CIE coordinates of white illumination, and (x_d, y_d) the CIE coordinate of dominated wavelength.

The obtained color purity for various Eu^{3+} concentrations has been reported in Table 1, with values in the range from 79% to 86%. Then the variation of the concentration causes a change in the chromaticity coordinate. This is mainly due to the variation in the ratios of the emission intensities due to the concentration extinction phenomenon. We compared the chromaticity coordinate and color purity of the ideal sample and the commercial Y$_2$O$_3$:Eu^{3+} phosphor to assess the quality of

the NYVO:xEu^{3+} phosphor. The calculated values are near to those of the commercial sample Y$_2$O$_2$S:Eu^{3+} (x = 0.622, y = 0.351).[39] The correlated color temperature (CCT) used to define the color temperature of a light source is given by:[40]

$$\text{CCT} = -449n^3 + 3525n^2 - 6823n + 5520.33 \tag{8}$$

With $n = (x - x_e)/(y - y_e)$ represents the epicenter of chromaticity and x_e = 0.3320 and y_e = 0.1858.

It should be noted that phosphors with CCT values lower than 3200 K are generally considered as hot light sources, while those with higher TCC values at 4000 K are considered to be cold in appearance. In the present work, the TCC values obtained are all less than 3200 K, which indicates that the NYVO:xEu^{3+} phosphor could be used for the diodes emitting warm white light (LED).

4.3 Thermal stability

Thermal stability is an important feature for lighting applications. A phosphor with high thermal stability is then highly demanded in the application of w-LED.[41] It should be noted that high-power LED chips can reach temperatures of 420 K. However, the luminescence intensity reduces significantly at this temperature. Fig. 10a displayed the PL spectra under 395 nm excitation of NYVO:0.15Eu^{3+} measured at various temperatures so as to determine the thermal stability of the sample. As can be seen, the profile of the PL emissions remain constant as the temperature rises, whereas the intensity of the transition gradually decreases as the temperature rises from 280 K to 440 K, due to thermal quenching. In addition, the response to temperature is different for the (VO$_4$)$^{3-}$ and Eu^{3+} bands. The (VO$_4$)$^{3-}$ band undergoes a sharp decline in intensity, whereas a slow reduction in intensity is noted for Eu^{3+} bands, as indicated in the histogram shown in Fig. S3.† At 440 K, the luminescence intensity remains at 77% compared to that obtained at T = 300 K this value is in the same order than that measured for the red commercial phosphorus Y$_2$O$_3$:Eu^{3+} (80%).[42] It can be concluded that our phosphors have good thermal stability.

Nonradiative relaxation causes thermal quenching of luminescence in most cases. The number of excited electrons increases as the temperature rises. The thermal activation process may be shown using the Arrhenius equation.

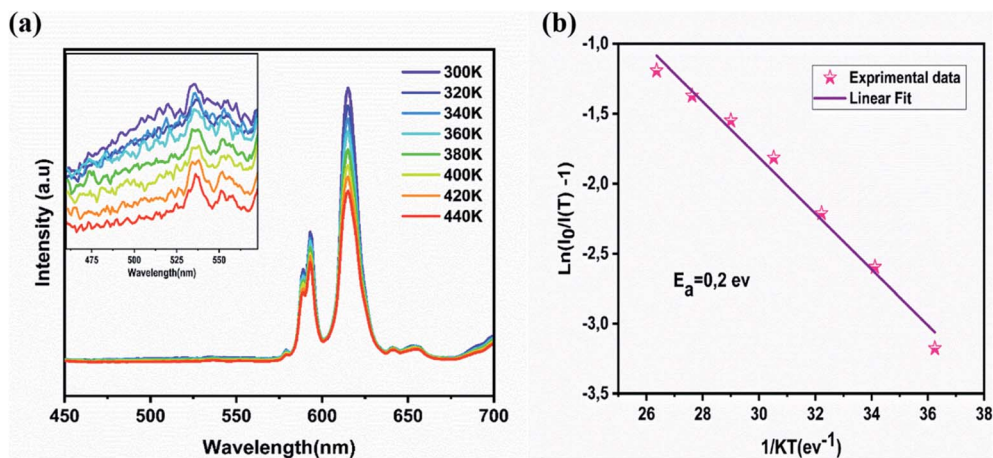$$I(T) = I_0 \left[1 + c \exp\left(-\frac{\Delta E_a}{K_B T} \right) \right]^{-1} \tag{9}$$

Fig. 10 (a) The temperature-dependent PL spectra (b) variations of $\ln((I_0/I) - 1)$ with $1/T$ in NYVO:xEu^{3+}.

where, I_0 signifies the intensity at room temperature, I refer to the luminescence intensity at various temperature, the Boltzmann constant is symbolized by k, C is the constant. Fig. 10b shows the plot of the relationship between $[(I_0/I) - 1]$ and $1/K_BT$, which corresponds to a linear function of slope ΔE. Fitting this curve allows us to estimate the activation energy at 0.2 eV. This value clearly confirms the high thermal stability of NYVO:0.15Eu^{3+} phosphor. Clearly, the thermal activation energy of NYVO:0.15Eu^{3+} is greater than that of certain previously reported phosphors, such as BaZrGe$_3$O$_9$:Eu^{3+} (0.18 eV),[43] Ba$_2$Y$_{2/3}$TeO$_6$:Eu^{3+} (0.15 eV),[44] Sr$_2$MgTeO$_6$:Eu^{3+} (0.27 eV),[45] LiSrBiTeO$_6$:Eu^{3+} (0.29 eV)[46] showing that NYVO:Eu^{3+} phosphor has strong thermal stability.

5. Temperature-sensing properties of NYVO:Eu^{3+}

Fig. 11 illustrates the PL spectra of NYVO:0.15Eu^{3+} at various temperatures under 375 nm excitation. It's clear that rising
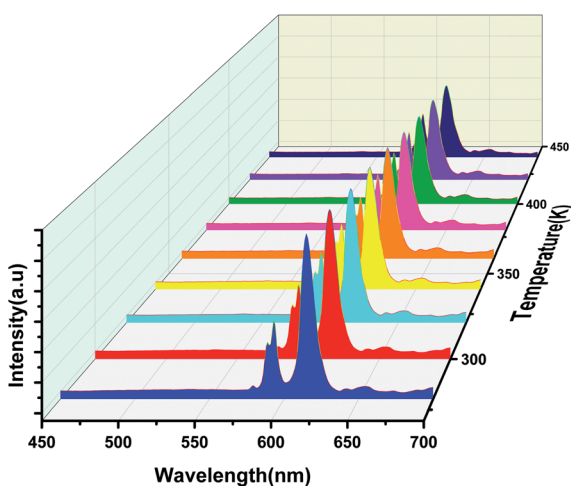

Fig. 11 Emission spectra of the NYVO:0.15Eu^{3+} phosphor for different temperatures under 375 nm excitation.

temperatures resulted in different behavior of Eu^{3+} and host emission intensities. This kind of variation in the intensity of these optical centers can be exploited for optical thermometry applications based on thermometric parameters Δ. For this, we have used the TeSen calculator which is a numerical program to calculate thermometric parameters.[47] Taking this into consideration, we advocated using Δ between the host band and the transition of Eu^{3+} as a temperature-dependent factor. The Δ approach removes temperature readout errors caused by changes in excitation intensity or detecting system, as well as nonhomogeneous distribution of the probe over the measuring surface, because the intensity ratio between two emission bands is derived from the same measurements.[48]

The LIRs between the vanadate band and the two most intense Eu^{3+} emission lines: LIR$_1$ ($I_{host}/I_{(^5D_0-^7F_1)}$) and LIR$_2$ ($I_{host}/I_{(^5D_0-^7F_2)}$) were calculated using TeSen 30 calculator (Fig. 12), developed by Kaczmarek et al..[47] For the NYVO:0.15Eu^{3+} sample, the LIRs ratios showed a monotonic rise along with the temperature decreasing. Here, we examined the LIRs of VO$_4$$^{3-}$ and Eu^{3+} emissions over the 280 K to 440 K and found that it can be approximated by the following equation:

$$\text{LIR} = \Delta = \frac{I_{host}}{I_{Eu^{3+}}} = \frac{\Delta_0}{1 + \beta \exp\left(\dfrac{\Delta E}{K_B T}\right)} \tag{10}$$

where Δ_0 is the thermometric parameter at $T = 0$ K; T is the absolute temperature (K); and ΔE is the activation energy of the non-radiative process, β is the ratio between the nonradiative rates (W_0 is at $T = 0$ K) and radiative rates (W_R).

Sensitivity was an important and prominent characteristic for quantitatively determining the suitability of materials as an optical sensor in practical applications. Furthermore, the absolute sensitivity (S_a) and relative sensitivity (S_r) may be calculated using the formula below.[15,49,50]

$$S_r = \frac{1}{\Delta}\frac{\delta\Delta}{\delta T} \quad S_a = \frac{\delta\Delta}{\delta T} \tag{11}$$

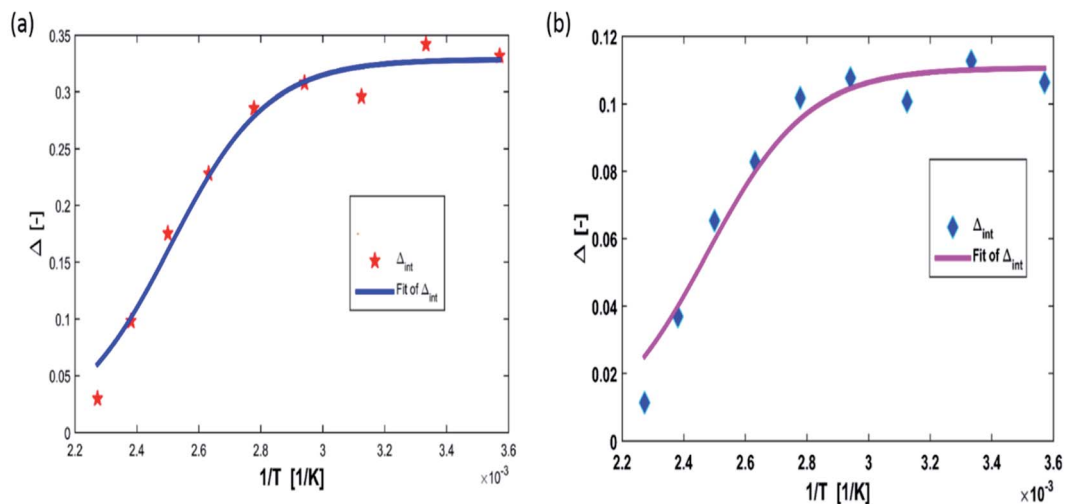Fig. 13a and b show the variations of absolute sensitivities with temperature. It indicates that S_a increases with

Fig. 12 Temperature evolution of luminescence intensity ratio (a) $\Delta_1 = \frac{I_{host}}{I_{^5D_0-^7F_1}}$ and (b) $\Delta_2 = \frac{I_{host}}{I_{^5D_0-^7F_2}}$ for NYVO:Eu^{3+}.
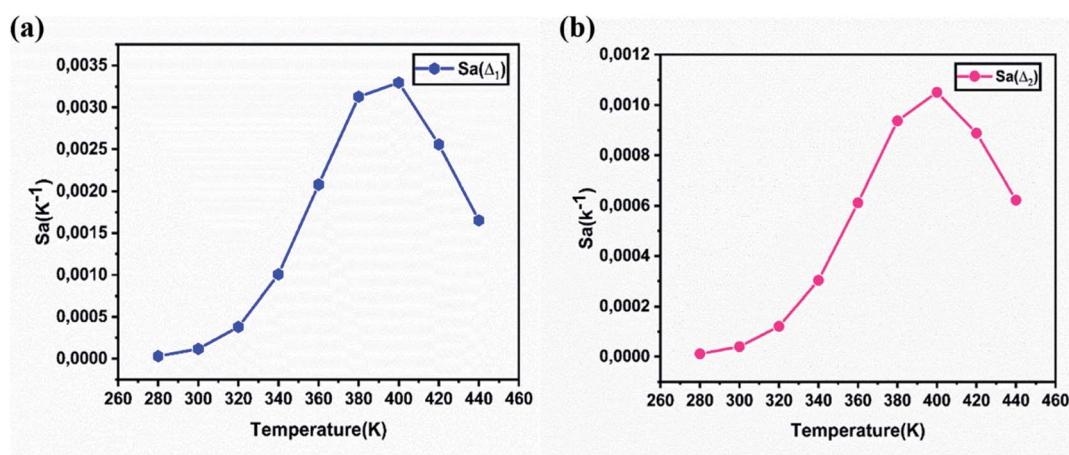

Fig. 13 The absolute sensitivity S_a calculated for NYVO:Eu^{3+} as a function of the temperature, corresponding to Δ_1 (a) and to Δ_2 (b).

temperature up to 400 K and after that decrease. The maximum absolute sensitivity was 0.0033 K^{-1} for Δ_1 ($I_{host}/I_{(^5D_0-^7F_1)}$) and 0.00105 K^{-1} for Δ_2 at 400 K respectively.

Fig. 14 show the relative sensitivity of NYVO:Eu^{3+} calculated for Δ_1 and Δ_2 ratios. As can be observed, increasing the temperature causes an increase in the S_r values. The maximum
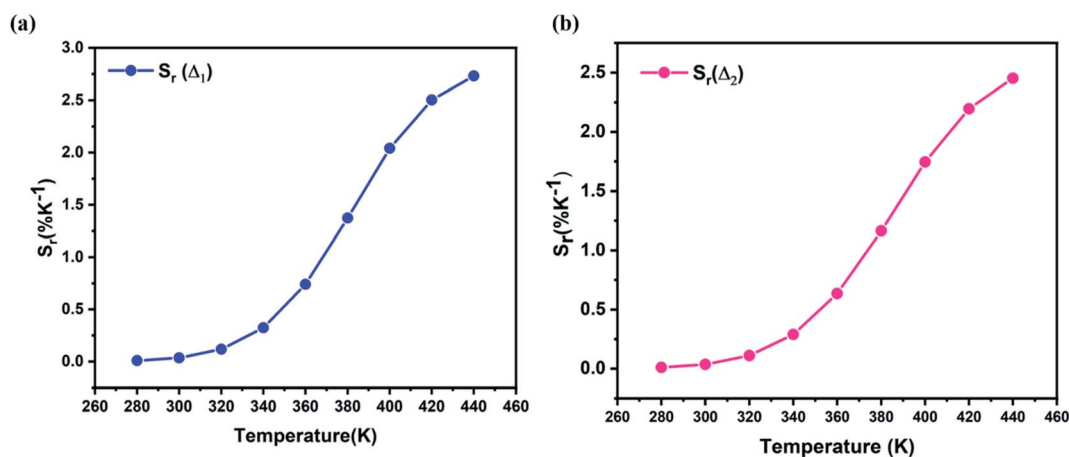

Fig. 14 The relative sensitivity S_r values corresponding to (a) Δ_1 (b) Δ_2 ratios at different temperatures.
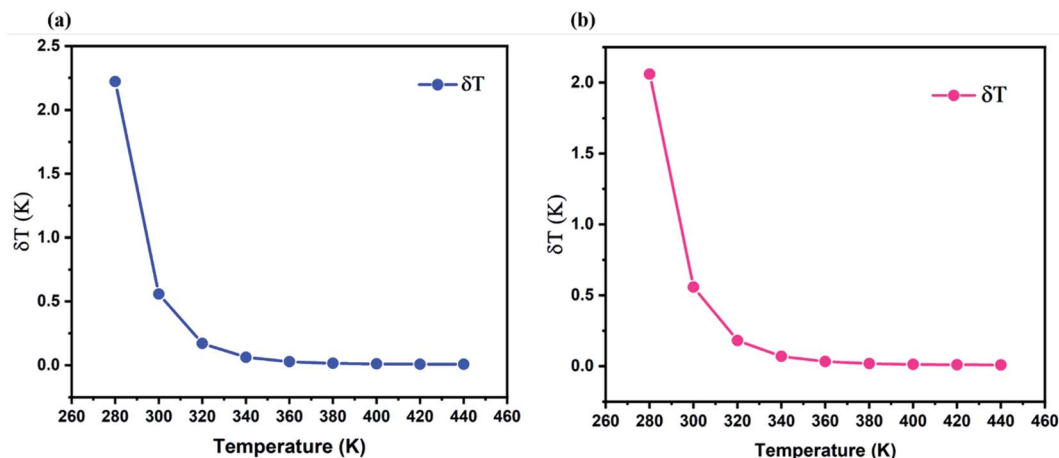
Fig. 15 Temperature uncertainty of NYVO:0.15Eu^{3+} corresponding to Δ_1 (a) and r Δ_2 (b).

Table 2 Temperature sensitivity comparison of phosphor

Compounds	T [K]	λ_{ex} [nm]	S_r [% K^{-1}]	S_a [K^{-1}]	Ref.
$Ca_2NaMg_2V_3O_{12}$:Eu^{3+}	303–503	335	1.686	0.0156	54
$Ba_3La(VO_4)_3$:Eu^{3+}	298–573	320	1.77	0.0515	8
YVO_4:Eu^{3+} 10 at%	298–473	618	1.08	0.00039	55
$Ca_5Mg_4V_6O_{24}$:Eu^{3+}	300–480	310	1.83	—	56
$CaEu_2(WO_4)_4$:Eu^{3+}	300–500	395	1.4	—	57
$Na_3Sc_2P_3O_{12}$:Eu^{2+}, Mn^{2+}	293–473	340	1.556	—	58
$NaEuF_4$:Eu^{3+}	298–523	394	0.43	—	59
$LuAG$:Eu^{3+}/Mn^{4+}	303–358	393	0.7	0.07	60
SnO_2:Eu^{3+}	298–623	250	1.83	0.0159	61
$Na_3Y(VO_4)_2$:Eu^{3+}	298–440		2.7	0.0033	This work
			2.4	0.0010	This work

relative sensitivity is determined to be 2.7% K^{-1} at 440 K for Δ_1 $\left(\dfrac{I_{host}}{I_{^5D_0-^7F_1}}\right)$ and 2.42% K^{-1} for Δ_2 $\left(\dfrac{I_{host}}{I_{^5D_0-^7F_2}}\right)$.

The temperature uncertainty (temperature resolution) (δT) defines the minimal change in temperature that represents a high difference in the examined parameter, which is an essential measure of the quality for a thermometer's performance.[51,52] δT was estimated using the first approach using the following formula:[53]

$$\delta T = \frac{\delta \Delta / \Delta}{S_r} \qquad (12)$$

where $\delta\Delta/\Delta$ is the relative uncertainty of Δ, the minimum temperature uncertainties are calculated to be 0.007 K (at 440 K) for Δ_1 and 0.008 for Δ_2 at 400 K, respectively (Fig. 15a and b).

The relative and absolute sensitivities calculated for NYVO:0.15Eu^{3+} phosphor is compared with those calculated in other hosts (Table 2). NYVO:0.15Eu^{3+} phosphors can then be employed for optical thermometry applications.

6. Conclusion

A new NYVO:Eu^{3+} phosphor was prepared using the sol–gel method. The NYVO mico powder crystallizes in a monoclinic system with particle size around 0.8 μm. The absorption measurements show the formation of the vanadate host by the presence of its characteristic band in the visible region related to VO_4^{3-} groups, and the energy gap was estimated to be around 3.15 eV. Under near-ultraviolet (UV) excitation, both the broadband emission from VO_4^{3-} groups and the sharp peak emissions from Eu^{3+} ions are observed. The highest luminescence intensity was achieved for an optimal europium concentration of 15% mol. The study of the chromaticity parameters gives a thermally stable hot emission in the red domain, with a color purity of about 85%. Eu^{3+}-doped NYVO phosphors were also tested as noncontact ratiometric luminescence thermometers. Notably, the optical thermometry of NYVO:Eu^{3+} was characterized based on the fluorescence intensity ratio of VO_4^{3-} and Eu^{3+} emissions in the 298–440 K range. The best room-temperature thermometric performance with a maximum absolute and relative sensitivities of 3.4% K^{-1} and 0.0032 K^{-1} respectively and a temperature uncertainty of 0.01 for the case of LIR$_2$ ($I_{host}/I_{(^5D0-^7F2)}$). The obtained results make Eu^{3+}-doped NYVO micro crystals as promising candidates for accurate contactless ratiometric temperature sensing and as a potential phosphor for light-emitting diodes (LED) applications.

Conflicts of interest

There are no conflicts to declare.

References

1 S. V. Eliseeva and J.-C. G. Bünzli, *Chem. Soc. Rev.*, 2010, **39**, 189–227.

2 K. Binnemans, *Chem. Rev.*, 2009, **109**, 4283–4374.

3 J.-C. G. Bünzli and C. Piguet, *Chem. Soc. Rev.*, 2005, **34**, 1048.

4 M. K. Hossain, S. Hossain, M. H. Ahmed, M. I. Khan, N. Haque and G. A. Raihan, *ACS Appl. Electron. Mater.*, 2021, **3**, 3715–3746.

5 K. Saidi and M. Dammak, *RSC Adv.*, 2020, **10**, 21867–21875.

6 K. Saidi and M. Dammak, *J. Solid State Chem.*, 2021, **300**, 122214.

7 E. Céspedes, J. M. Byrne, N. Farrow, S. Moise, V. S. Coker, M. Bencsik, J. R. Lloyd and N. D. Telling, *Nanoscale*, 2014, **6**, 12958–12970.

8 P. Yang, L. Li, Y. Deng, Y. Wang, S. Jiang, X. Luo, G. Xiang, Y. Lu and X. Zhou, *Dalton Trans.*, 2019, **48**, 10824–10833.

9 C. D. S. Brites, A. Millán and L. D. Carlos, in *Handbook on the Physics and Chemistry of Rare Earths*, Elsevier, 2016, vol. 49, pp. 339–427.

10 C. D. S. Brites, P. P. Lima, N. J. O. Silva, A. Millán, V. S. Amaral, F. Palacio and L. D. Carlos, *Nanoscale*, 2012, **4**, 4799.

11 J. Cao, D. Xu, F. Hu, X. Li, W. Chen, L. Chen and H. Guo, *J. Eur. Ceram. Soc.*, 2018, **38**, 2753–2758.

12 J. Cao, X. Li, Z. Wang, Y. Wei, L. Chen and H. Guo, *Sens. Actuators, B*, 2016, **224**, 507–513.

13 D. K. Chatterjee and Z. Yong, *Nanomedicine*, 2008, **3**, 73–82.

14 C. Shen, T. K. Ng, J. T. Leonard, A. Pourhashemi, H. M. Oubei, M. S. Alias, S. Nakamura, S. P. DenBaars, J. S. Speck, A. Y. Alyamani, M. M. Eldesouki and B. S. Ooi, *ACS Photonics*, 2016, **3**, 262–268.

15 K. Soler-Carracedo, I. R. Martín, F. Lahoz, H. C. Vasconcelos, A. D. Lozano-Gorrín, L. L. Martín and F. Paz-Buclatin, *J. Alloys Compd.*, 2020, **847**, 156541.

16 N. M. Bhiri, M. Dammak, M. Aguiló, F. Díaz, J. J. Carvajal and M. C. Pujol, *J. Alloys Compd.*, 2020, **814**, 152197.

17 Y. Hua and J. S. Yu, *J. Mater. Sci. Technol.*, 2021, **91**, 148–159.

18 Y. Gao, F. Huang, H. Lin, J. Zhou, J. Xu and Y. Wang, *Adv. Funct. Mater.*, 2016, **26**, 3139–3145.

19 D. Chen, S. Liu, Y. Zhou, Z. Wan, P. Huang and Z. Ji, *J. Mater. Chem. C*, 2016, **4**, 9044–9051.

20 D. K. Amarasinghe and F. A. Rabuffetti, *Inorg. Chem.*, 2021, **60**, 3165–3171.

21 N. Krutyak, D. Spassky, V. Nagirnyi, A. V. Antropov and D. V. Deyneko, *Opt. Mater.*, 2021, **122**, 111738.

22 F. Ayachi, K. Saidi, W. Chaabani and M. Dammak, *J. Lumin.*, 2021, **240**, 118451.

23 K. Saidi, M. Dammak, K. Soler-Carracedo and I. R. Martín, *J. Alloys Compd.*, 2022, **891**, 161993.

24 L. A. Jacob, S. Sisira, K. Thomas, D. Alexander, P. R. Biju, N. V. Unnikrishnan and C. Joseph, *J. Solid State Chem.*, 2019, **280**, 120998.

25 L. A. Jacob, S. Sisira, K. P. Mani, K. Thomas, D. Alexander, P. R. Biju, N. V. Unnikrishnan and C. Joseph, *J. Lumin.*, 2020, **223**, 117169.

26 M. M. Kimani, C. D. McMillen and J. W. Kolis, *J. Solid State Chem.*, 2015, **226**, 320–325.

27 R. Salmon, C. Parent, G. Le Flem and M. Vlasse, *Acta Crystallogr., Sect. B: Struct. Crystallogr. Cryst. Chem.*, 1976, **32**, 2799–2802.

28 Sk. K. Hussain, H. S. Go, J. J. Han, H. Patnam, G. Nagaraju and J. S. Yu, *J. Alloys Compd.*, 2019, **805**, 1271–1281.

29 K. Saidi, W. Chaabani and M. Dammak, *RSC Adv.*, 2021, **11**, 30926–30936.

30 I. E. Kolesnikov, A. V. Povolotskiy, D. V. Tolstikova, A. A. Manshina and M. D. Mikhailov, *J. Phys. D: Appl. Phys.*, 2015, **48**, 075401.

31 I. E. Kolesnikov, D. V. Mamonova, E. Lähderanta, A. V. Kurochkin and M. D. Mikhailov, *J. Lumin.*, 2017, **187**, 26–32.

32 K. Binnemans, *Coord. Chem. Rev.*, 2015, **295**, 1–45.

33 H. Peng, S. Huang, L. Sun and C. Yan, *Phys. Lett. A*, 2007, **367**, 211–214.

34 Q. Liu, M. Zhang, Z. Ye, X. Wang, Q. Zhang and B. Wei, *Ceram. Int.*, 2019, **45**, 7661–7666.

35 M. Fhoula and M. Dammak, *J. Lumin.*, 2019, **210**, 1–6.

36 Z. Yahiaoui, M. A. Hassairi, M. Dammak and E. Cavalli, *J. Alloys Compd.*, 2018, **763**, 56–61.

37 V. Mahalingam and J. Thirumalai, *RSC Adv.*, 2016, **6**, 80390–80397.

38 M. Fhoula, T. Koubaa and M. Dammak, *Opt. Laser Technol.*, 2020, **130**, 106352.

39 Y. Hua, Sk. K. Hussain and J. S. Yu, *Ceram. Int.*, 2019, **45**, 18604–18613.

40 C. S. McCamy, *Color Res. Appl.*, 1992, **17**, 142–144.

41 J. Qin, C. Hu, B. Lei, J. Li, Y. Liu, S. Ye and M. Pan, *J. Mater. Sci. Technol.*, 2014, **30**, 290–294.

42 S. Som, S. Das, S. Dutta, H. G. Visser, M. K. Pandey, P. Kumar, R. K. Dubey and S. K. Sharma, *RSC Adv.*, 2015, **5**, 70887–70898.

43 Q. Zhang, X. Wang, X. Ding and Y. Wang, *Inorg. Chem.*, 2017, **56**, 6990–6998.

44 S. C. Lal, J. Isuhak Naseemabeevi and S. Ganesanpotti, *Mater. Adv.*, 2021, **2**, 1328–1342.

45 J. Liang, S. Zhao, X. Yuan and Z. Li, *Opt. Laser Technol.*, 2018, **101**, 451–456.

46 J. He, Z. Gao, S. Liu, J. H. Jeong, R. Yu and B. Deng, *J. Lumin.*, 2018, **202**, 7–12.

47 A. M. Kaczmarek, R. Van Deun and M. K. Kaczmarek, *Sens. Actuators, B*, 2018, **273**, 696–702.

48 M. Sekulić, V. Đorđević, Z. Ristić, M. Medić and M. D. Dramićanin, *Adv. Opt. Mater.*, 2018, **6**, 1800552.

49 S. A. Wade, S. F. Collins and G. W. Baxter, *J. Appl. Phys.*, 2003, **94**, 4743–4756.

50 K. Maciejewska, A. Bednarkiewicz, A. Meijerink and L. Marciniak, *J. Phys. Chem. C*, 2021, **125**, 2659–2665.

51 J.-C. G. Bünzli, in *Handbook on the Physics and Chemistry of Rare Earths*, Elsevier, 2016, vol. 50, pp. 141–176.

52 C. D. S. Brites, A. Millán and L. D. Carlos, in *Handbook on the Physics and Chemistry of Rare Earths*, Elsevier, 2016, vol. 49, pp. 339–427.

53 S. N. Baker, T. M. McCleskey and G. A. Baker, in *Ionic Liquids IIIB: Fundamentals, Progress, Challenges, and Opportunities*, American Chemical Society, 2005, vol. 902, pp. 171–181.

54 H. Zhou, N. Guo, X. Lü, Y. Ding, L. Wang, R. Ouyang and B. Shao, *J. Lumin.*, 2020, **217**, 116758.

55 I. E. Kolesnikov, A. A. Kalinichev, M. A. Kurochkin, D. V. Mamonova, E. Yu. Kolesnikov and E. Lähderanta, *J. Phys. Chem. C*, 2019, **123**, 5136–5143.

56 N. Zhang, J. Li, J. Wang, R. Shi, L. Chen, A. Zhang and P. Yang, *RSC Adv.*, 2019, **9**, 30045–30051.

57 K. W. Meert, V. A. Morozov, A. M. Abakumov, J. Hadermann, D. Poelman and P. F. Smet, *Opt Express*, 2014, **22**, A961–A972.

58 X. Zhang, Z. Zhu, Z. Guo, Z. Sun and Y. Chen, *Chem. Eng. J.*, 2019, **356**, 413–422.

59 Y. Tian, B. Tian, C. Cui, P. Huang, L. Wang and B. Chen, *Opt Express*, 2014, **39**, 4164–4167.

60 B. Yan, Y. Wei, W. Wang, M. Fu and G. Li, *Inorg. Chem. Front.*, 2021, **8**, 746–757.

61 S. Das, S. Som, C.-Y. Yang and C.-H. Lu, *Mater. Res. Bull.*, 2018, **97**, 101–108.